Performance degradation due to anodic failure mechanisms in lithium-ion batteries

Abhishek Sarkar[1], Ikenna Nlebedim[1,*], Pranav Shrotriya[2]

1. Critical Materials Institute, Ames Laboratory, United States DOE, Ames, IA – 50010, USA
2. Department of Mechanical Engineering, Iowa State University, Ames, IA – 50010, USA

Abstract:

We report a mechano-chemical model for anodic degradation during fast-charging of nickel-manganese-cobalt (NMC)/graphite (C) cell due to SEI growth, lithium plating/stripping, dead lithium storage, and film fracture of composite SEI and plated lithium film. Degradation of the battery is analyzed for a range of charging rates from 1 – 6 C-rates, and the influence of plating mechanisms – lithium plating and dead lithium deposition and recovery during stripping – on the film resistance of the anode are accounted for in the model. Dynamic evolution of the interfacial properties is modeled using rule-of-mixture approach. Model predictions of plating associated stress fields are used to compute critical energy release rate for film cracking. The results indicate an increased tendency of fracture for thinner SEI film with lithium plating at higher charging rates. The process of reforming the cracked film absorbs a significant portion of the electrode current thereby reducing the cell capacity and plating efficiency. The mechano-chemical model provides an extensive analytical framework for understanding the synergistic coupling of anodic degradation mechanisms, prognosticating conditions of SEI failure, and evaluating the capacity fade and efficiency of lithium-ion battery.

Keywords: *Anodic degradation; Lithium plating; Dead lithium storage; SEI fracture; Capacity fade*

1. Introduction

Advancements in electric vehicles industry and growth of electronic technologies require compact and energy-dense batteries, with long cycle life (~10 – 15 years), and, more importantly, fast-charging capabilities [1–4]. Over the past several decades, lithium-ion batteries with graphite electrodes have been the dominant energy storage technology with higher efficiency, power density and calendar life compared to other rechargeable batteries, like nickel-cadmium or lead-acid [5,6]. However, it has been challenging to meet the requirements of fast-charging and high-capacity battery in electric vehicles (EV), due to synergistic interaction of several degradation mechanisms resulting in increase in cell resistance, and reduction of cycle-life and columbic efficiency [7–9].

Anodic materials of lithium-ion battery are more susceptible to ageing phenomena due to the open circuit potential (OCV) being closer to lithium metal [10]. The lower OCV for graphite electrode increases the tendency of electrolyte to react with the graphite surface, thus depleting active lithium from the electrolyte in the form of irreversible or reversible film deposition [11]. One of the primary ageing mechanism in lithium-ion batteries is solid electrolyte layer (SEI) formation and growth on anode particles [12–14]. SEI layer is an ionically conductive but electronically insulating film, formed when the redox potential of the anode lies outside the potential range of the battery [15]. The initial SEI layer, formed when the anodic material comes in contact with electrolyte, acts as a passivation film which protects the electrode particle. However, continued evolution of SEI layer consumes the active material and increases the resistance of the anode particle, resulting in gradual decay of battery capacity with each cycle [16,17]. Chemical composition of the electrolyte impacts the impedance of the SEI film [17,18]. Selection of the electrolyte/electrode chemistry that reduces the impedance of the SEI film has been reported to retard the decomposition of the active lithium salt (e.g. $LiPF_6$), leading to improved electrochemical performance [19,20]. During lithiation, the electrode particles expand leading to development of mechanical stresses in the particle surface and core [21]. High charging

load on the battery amplifies the stress build-up on the electrode/electrolyte interface causing fracture of the SEI film, exposing new anode surface, reforming SEI and reducing capacity of the battery [22,23].

Lithium plating on anode particles during conditions of fast charging, low temperature, and over-charging leads to a more drastic decay in the cell capacity [10]. Ultra-high-precision columetric, calorimetric, and post mortem SEM imaging reveal that drastic decay is associated with electrodeposition of metallic lithium on the anode electrode/electrolyte interface during charging [24–26]. Further investigations of anode potential, with reference to lithium metal as counter, establish that the lithium plating mechanisms occur when the anode potential drops below 0 V (vs. Li/Li^+) during charging [27,28]. The metallic lithium deposits on the anode particles during this potential window, and gets stripped-off when the anodic potential becomes positive [29,30]. However, all of the plated lithium is not completely recovered. The plated lithium may either go back into the electrolyte solution and reversibly intercalate with anode particle, or irreversibly deposit as new SEI layer and/or get trapped as dead-lithium on the anode surface [31–33]. In addition to the capacity loss, the uncontrolled dendritic lithium growth could possibly pierce the separator membrane leading to thermal runaway due to short-circuit between the electrodes.

Computational modelling of the battery degradation due to lithium plating is useful in predicting the capacity loss and cycle life, and as well as for prognosticating the conditions to reduce electrochemical degradation of batteries. Yang et al. 2017 [34] have modeled the lithium plating mechanism with SEI growth and shown a transition of rate of capacity fading from linear to non-linear during cell cycling. In a follow-up paper, Yang et al. [32] have also modeled the lithium plating and stripping to predict the experimentally observed voltage plateau during the relaxation period after charging cycle [35]. A low temperature lithium plating analysis has been performed to predict the lithium deposition, aided with NMR to characterize the SEI film composition at sub-zero conditions [36]. Thermal-electrochemical coupled analysis at sub-zero

conditions has shown an increased irreversible lithium plating at low temperatures, which is countered by a rise in the cell temperature during charging [37,38]. A model by Müller et al. 2019 [39], demonstrates the sudden-death effect due to combined SEI and lithium metal deposition and second life reuse applications of lithium battery. In these papers, the authors have provided a detailed mathematical scheme for lithium plating and SEI growth but did not model the irreversible losses of lithium in the plated film during stripping process by SEI growth, dead lithium loss and film fracture. Furthermore, the variation of film resistance due to deposition of conductive metallic lithium in the electrically insulating SEI film were not discussed.

In this study, we model the interfacial kinetics of a composite film composed of SEI and metallic lithium to simulate the irreversible lithium loss during fast charging. A single particle with electrolyte model was used to simulate the electrochemical behavior of an NMC/C cell over a range of charging rates (1 – 6 C). The electrochemical kinetics for lithium intercalation was coupled with kinetic models for lithium plating, stripping and SEI growth. A novel approach was introduced in this study to model the change in film resistance during lithium plating/stripping. Rule-of-mixture (ROM) approach for transversely aligned composites was used to model the electromechanical response of the composite film during fast charging accounting for the contribution from metallic lithium in the SEI film. A thin film based mechanistic model was used to predict the film stress and fracture condition. The coupled mechano-chemical model was used to predict the plating efficiency and relative capacity of the battery. The modeling predictions can help to develop diagnostic and prognostic tools as part of battery management systems. Such tools can help predict the remaining useful life and state-of-health of lithium batteries [40]. Consequently, the embedded energy in the sourcing of raw materials, design and development of batteries can be maximized by identifying suitable applications for battery second life.

The organization of the remaining part of the manuscript is as follows: first, a *Mathematical Model* section is introduced to detail the mathematical framework on which the anodic degradation mechanisms were based. The section describes the mathematical basis for five types of models

including electrochemical, anodic reaction kinetic, film growth and resistance, fracture mechanics, capacity and efficiency models. Next, a *Result and Discussion* section is presented which describes the results from the model predictions and inferences made in order to provide physical interpretation of the modeling results. Finally, a *Conclusion* section of the key findings, based on the model predictions is provided to explain the synergistic interaction between different mechanisms that result in anodic degradation in Li-ion batteries.

2. Mathematical Model

Figure 1a presents a schematic representation of the anodic degradation under the condition of fast charging considered in the model. The effects of overcharging and undercharging are not considered. The anodic degradation generally occurs with the formation and growth of SEI layer that consumes active lithium from the electrolyte. However, under conditions of fast charging where the anodic potential becomes negative, lithium metal starts to plate on the graphite, along with the SEI film.

At the end of charging, the anodic potential becomes positive, and a portion of the plated lithium gets stripped off during the relaxation period. The stripped lithium intercalates reversibly with the anode, and this phenomenon is observed electrochemically as a plateau in the voltage-time curve. While the remaining plated lithium either reacts with the electrolyte to form new SEI or gets trapped in between SEI layers and becomes unavailable for reaction. In both cases, the irreversible loss of lithium causes capacity fading of the battery. Additionally, tensile stresses induced fracture in the SEI film due to particle expansion may also contribute to lithium consumption due to formation of new SEI layers on freshly exposed anode surfaces. The following sections describe the mathematical analysis for the coupled mechano-chemical degradation model. All symbols are defined in the nomenclature section.

2.1 Electrochemical model:

Following the single particle model [41], a spherical electrode particle is considered to freely expand in a pool of electrolyte. The mass diffusion in electrode particles is modeled using Fick's Diffusion Law Eqs. (1) and (2).

$$\frac{\partial c_s}{\partial t} = \frac{D_s}{r^2}\frac{\partial}{\partial r}\left(r^2 \frac{\partial c_s}{\partial r}\right) \tag{1}$$

$$-D_s \frac{\partial c_s}{\partial r} = \frac{i_{el}}{F} \tag{2}$$

The solid phase lithium-ion concentration (c_s) changes with intercalating lithium-ion flux ($j_{el} = i_{el}/F$) at the particle surface. As the particle lithiates, it expands by absorbing the lithium-ion from the electrolyte phase. The mass diffusion of the electrolyte is governed by diffusion of ions through the electrode and separator film, plus electromigration due to current flux at the particle interface Eqs. (3), (4) and (5).

$$\varepsilon \frac{\partial c_e}{\partial t} = \varepsilon D_e \nabla^2 c_e + \frac{(1 - t_+)\nabla . i_e}{F} \tag{3}$$

$$-D^-_{e,int} \frac{\partial c_e}{\partial x}\Big|^-_{int} = -D^+_{e,int} \frac{\partial c_e}{\partial x}\Big|^+_{int} \tag{4}$$

$$c_e|^-_{int} = c_e|^+_{int} \tag{5}$$

The total exchange current density (i_{tot}), available at the particle level, is proportional to the gradient of the solid and electrolyte phase current densities. From current balance, the total input current density (I_{tot}) is split between solid (I_s) and electrolyte (I_e) phase current densities Eqs. (6) and (7).

$$I_s + I_e = I_{tot} \tag{6}$$

$$\nabla . I_s = -\nabla . I_e = -a . i_{tot} \tag{7}$$

Here, the gradient parameter $a = 3\varepsilon/R$. By using Ohm's law, the electrode and electrolyte potential, σ_e and σ_s, are estimated from the current densities as in eqs. (8) and (9), respectively.

$$\sigma_e \frac{\partial \phi_e}{\partial x} = -I_e + \sigma_e \frac{2RT}{F}(1 - t_+)\left(1 + \frac{\partial ln f_\pm}{\partial c_e}\right)\frac{\partial ln c_e}{\partial x} \tag{8}$$

$$\sigma_s \frac{\partial \phi_s}{\partial x} = -I_s \tag{9}$$

2.2 Anodic reaction kinetic model:

At the particle level, the exchange current density from the lithium-ion flux (i_{tot}) is a superposition of flux contributions from electrode intercalation (i_{el}), SEI growth (i_{SEI}), lithium plating (i_{pl}) and stripping (i_{st}) mechanisms, and formation of new film to reform cracked SEI film (i_{cr}), as captured in Eq. (10).

$$i_{tot} = i_{el} + i_{SEI} + i_{pl} + i_{st} + i_{cr} \tag{10}$$

The electrode exchange current (i_{el}) (Eq. (11)) is modeled using the Butler Volmer kinetic formulation [42] and it is affected by the concentration of lithium-ions on the surface of the particle.

$$i_{el} = 2Fk_{el}\sqrt{c_{s,surf}\left(c_{s,max} - c_{s,surf}\right)c_e}\,\sinh\left(\frac{\alpha F}{\mathcal{R}T}\left(\eta - U_{OCP} - \mathbb{R}_{film}i_n\right)\right) \tag{11}$$

Here, the anodic potential ($\eta = \Phi_s - \Phi_e$) is affected by the resistance of the deposited film ($\mathbb{R}_{film}$) on the surface of the particle. The SEI current density (i_{SEI}) is governed by the Tafel kinetics as the reaction is dominant on the anode side of the redox potential (see Eq. (12)) [43].

$$i_{SEI} = -Fk_{SEI}c_{EC}^{surf}\exp\left(-\frac{\alpha_{SEI}F}{\mathcal{R}T}\left(\eta - U_{SEI} - \mathbb{R}_{film}i_n\right)\right) \tag{12}$$

The concentration of ethylene carbonate, a solvent in the electrolyte, at the surface of the film/electrolyte interface (c_{EC}^{surf}) drives the SEI current causing film growth. Fick's first law of diffusion is used to model the transport of ethylene carbonate concentration from the film to the bulk across the SEI plus plated lithium layer (Eq. (13)).

$$-D_{EC}\frac{\partial c_{EC}^{surf}}{\partial \delta_{film}} = \frac{i_{SEI}}{F} \tag{13}$$

The diffusion is assumed to be at steady state considering the low mass diffusivity (D_{EC}~10^{-17}) of lithium ions through the SEI film. The plating current is modeled using Butler Volmer formulation with the electrolyte concentration driving the current. The formulation is developed

such that the plating would initiate only when the anode potential becomes negative (Eq. (14)) [36].

$$i_{pl} = \min\left(0{,}2Fk_{pl}\sqrt{c_e}\sinh\left(\frac{\alpha_{pl}F}{\mathcal{R}T}\left(\eta - U_{pl} - \mathbb{R}_{film}\, i_n\right)\right)\right); \eta < 0 \qquad (14)$$

Since the plated film is metallic lithium, the OCP for plating (U_{pl}) is 0 V. The stripping occurs after the plating process during the relaxation period.

$$i_{st} = \max\left(0{,}2Fk_{pl}\sqrt{c_e}\sinh\left(\frac{\alpha_{pl}F}{\mathcal{R}T}\left(\eta - \mathbb{R}_{film} i_n\right)\right) m_{pl}/\max(m_{pl})\right);\ \eta > 0, \max\left(m_{pl}\right) > 0 \qquad (15)$$

In Eq. (15), the stripping current initiates when $\eta > 0$ and some amount of lithium metal (m_{pl}) has deposited in the form of plated film on the electrode particle ($\max\left(m_{pl}\right) > 0$) [44]. The geometric and electrochemical properties for the model are recorded in Table 1.

Table 1. Design and electrochemical properties of electrode in NMC/C lithium-ion cell used in simulation.

Properties	**Anode**	**Cathode**
Particle Radius, R (μm)	12.5 [36]	5 [36]
Electrode thickness. l (μm)	33 [36]	32 [36]
Diffusivity, D ($m^2\ s^{-1}$)	30×10^{-14} [36]	50×10^{-14} [36]
Porosity, ε (1)	0.360 [36]	0.243 [36]
Electrode kinetic parameter, k_{el} ($m^{5/2}mol^{-1/2}s^{-1}$)	2.43×10^{-11} [36]	1.02×10^{-11} [36]
Open circuit potential, U_{OCP} (V)	Refer Ge et al. 2017 [36]	Refer Ge et al. 2017 [36]
Butler Volmer parameter, α (1)	0.5	0.5
Maximum lithium concentration, $c_{s,max}$ (mol/m^3)	31542 [36]	49668 [36]
Initial SOC (1)	0.025[ad]	0.950[ad]
Partial molar volume, Ω_n ($m^3\ mol^{-1}$)	8.9×10^{-6} [45]	–
	SEI	**Plated lithium**
Kinetic Parameter, k_{SEI}, k_{pl} ($m\ s^{-1}, mol^{1/2}s^{-1}m^{-1/2}$)	1×10^{-12} [36]	2.23×10^{-7} [36]

Initial thickness (nm)	10[ad]	0[ad]
SEI diffusivity ($m^2\ s^{-1}$)	4.90×10^{-17} [46]	–
Initial ethylene carbonate concentration, c_{EC}^0 ($mol\ m^{-3}$)	4541 [34]	–
Electrolyte concentration, c_e ($mol\ m^{-3}$)	–	1000[ad]
Dead lithium factor, ξ (1)		0.01[ad]
Open circuit potential (OCP), U (V)	0.4 [34]	0
Butler Volmer parameter, α (1)	1.0	0.5
Density, ρ ($kg\ m^{-3}$)	1690 [43]	534 [47]
Molar mass, M ($kg\ mol^{-1}$)	0.162 [43]	0.007 [47]

[ad] Adjusted or assumed for the model

2.3 Film growth and resistance model:

The growth in thickness of the plated film during plating (reduction during stripping) is approximated using Fick's second law of diffusion with a source term accounting from the in-flux of plated lithium (out-flux of stripped lithium) based on the plating current density (stripping current density), see Eq. (16).

$$\frac{\partial \delta_{Li}}{\partial t} = -\frac{i_{pl}(or\ i_{st})M_{pl}}{F\rho_{pl}} \tag{16}$$

Similarly, the change in thickness of SEI film with time is approximated with a source term based on the SEI current density, as in Eq. (17).

$$\frac{\partial \delta_{SEI}}{\partial t} = -\frac{i_{SEI}M_{SEI}}{F\rho_{SEI}} \tag{17}$$

The mass deposited for the plated lithium is calculated ($m_{pl} = 4\pi R_n^2 \delta_{pl}\rho_{pl}$) and used to estimate the stripping current.

Experimental investigations have reported the presence of irreversible metallic lithium in the SEI layer [10]. A fraction of the plated layer gets coated by the SEI material during fast charging. The SEI prevents the metallic lithium from further reaction or intercalation. Furthermore, under conditions of mechanical stress from fast charging plated lithium could chip off from the film into

the electrolyte. In both cases the metallic lithium is unavailable for further intercalation and accounts for capacity loss of the battery. The mass of dead lithium is accounted by the fraction (ξ) , as in Eq. (18).

$$m_{pl,dead} = \xi \max(m_{pl}) \tag{18}$$

The film grows as a composite of lithium metal (discontinuous phase) in the SEI (matrix phase) with the total film thickness ($\delta_{film} = \delta_{SEI} + \delta_{pl} + \delta_{pl,dead}$). In the literature, the film resistance has been modeled either as a series sum of resistance between SEI and plated lithium materials [34,36,39] or just the SEI film resistance [37,38]. The film resistance has been predicted to increase negligibly or not increase at all after lithium metal deposition. However, electrochemical impedance spectroscopic (EIS) investigations have established that lithium plating reduces the film resistance due to metallic lithium being more conductive than the SEI film [48,49]. Assuming no dead-mass of lithium during the stripping process, the resistance is regained as the metallic lithium dissolves out and would possibly exceed the film resistance before plating due to SEI film growth during this time period. If some lithium are not stripped, e.g. trapped dead lithium in the SEI layers, the resistance restoration will be slightly lower than the condition before plating.

Rule-of-mixture (ROM) approaches are the widely used technique to predict various electro-thermo-mechanical properties in composite films [50,51]. These methods use weighted average to provide the upper and lower bound of composite properties based on the orientation of the particulate/fiber phase in the matrix. A major assumption in the ROM models is the homogeneity and periodicity of the fiber phase in the matrix. Hashin-Shtrikman lower bound formulation (for transverse aligned composite) is used to model the equivalent film conductivity (κ_{film}) [52,53] , as in Eq. (19). This provided a physically realizable reduction in the film resistance ($\mathbb{R}_{film}$) without short-circuiting the ionic pathway (Eq. (20)).

$$\kappa_{film} = \kappa_{SEI} + \phi_{pl}\left(\frac{1}{\kappa_{SEI} - \kappa_{pl}} + \frac{\phi_{SEI}}{3\kappa_{SEI}}\right)^{-1} \tag{19}$$

$$\mathbb{R}_{film} = \frac{\delta_{film}}{\kappa_{film}} \tag{20}$$

2.4 Fracture mechanics model:

During lithiation, the electrode particles expand freely in the electrolyte. The stresses developed in the electrode occurs due to the concentration gradient of lithium-ion within the particle. Since there is no lithium concentration in the surface film, the expanding particle exerts a tensile hoop stress in the film (Fig. 1a) [23]. The tensile hoop stress is developed from the strain on the particle surface during expansion ($\varepsilon_{film} = \frac{\Omega_n}{R_n^3}\int_0^{R_n} \tilde{c}r^2 dr$). For a spherical particle the film stress is given below in Eq. (21).

$$\sigma_{film} = \frac{\bar{E}_{film}}{(1 - \nu_{film})}\frac{\Omega_n}{R_n^3}\int_0^{R_n} \tilde{c}r^2 dr \tag{21}$$

As the SEI film grows with plated lithium deposited in the matrix, the equivalent stress state of the system changes depending on the phase fractions of SEI (ϕ_{SEI}) and metallic lithium (ϕ_{pl}) in the film. From the conductivity model, we establish that the plated lithium phase is transversely oriented in the film and thus perpendicular to the loading direction (Fig. 1b). A ROM model for transversely loaded composite is used to evaluate the equivalent mechanical properties ($X = \bar{E}, \nu$) for the composite film (Eq. (22) nd (23)).

$$X_{film}^{-1} = \left[\frac{\phi_{SEI}}{X_{SEI}} + \frac{\phi_{pl}}{X_{pl}}\right]^{-1} \tag{22}$$

$$\sigma_{c,film} = \left[1 - \left(\sqrt{\phi_{pl}} - \phi_{pl}\right)\left(1 - \frac{\bar{E}_{SEI}}{\bar{E}_{film}}\right)\right]\sigma_{c,SEI} \tag{23}$$

For a transversely loaded composite, the critical tensile strength for film is lower than that for the matrix phase (Fig. 1c) [50,54]. Assuming the ratio of deposited film thickness to particle radius is very small, we model the fracture with thin film formulation for through film crack [55].

$$G_{1,film} = \frac{\pi c_e^2 \sigma_{film}}{2\bar{E}_{film}} \delta_{film} \tag{24}$$

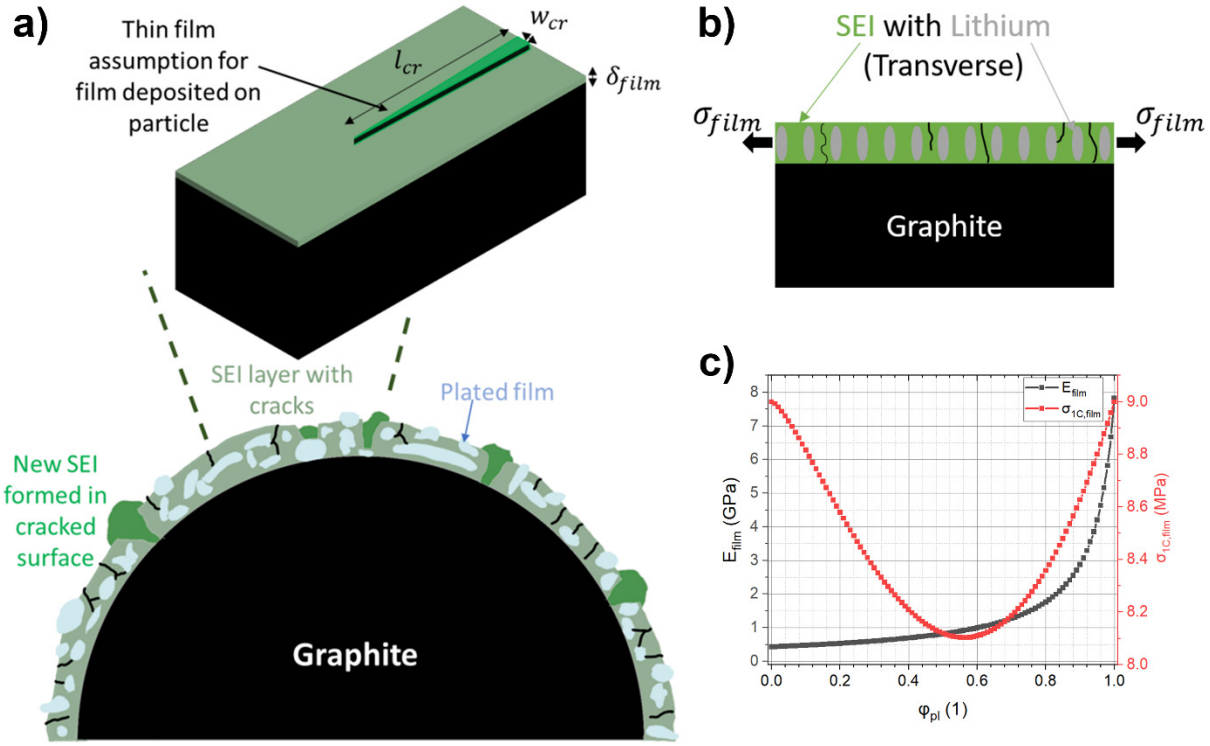

Figure 1. a) Schematic for anodic degradation representing SEI growth with lithium plating and film cracking, b) Film stress and composite model, and c) Prediction of mechanical properties for composite SEI and plated lithium.

Here, c_e is a constant (= 1.1215). The critical strain energy for the film ($G_{1C,film}$) is calculated using Eq. 24 by replacing $\sigma_{film} = \sigma_{c,film}$ and $\delta_{film} = \delta_{film,cr}$. Under the condition $G_{1,film} > G_{1C,film}$, the film will fracture (Fig. 1a) and crack will propagate along the surface of the film. Since, the crack generally propagates through the matrix phase (weaker phase), the surface energy of the SEI film is released to form two new cracked surfaces. The total length of the all the cracks (l_{cr}) is evaluated as follows in Eq. (25).

$$G_{1,film}(4\pi R_n^2) = 2\gamma l_{cr} \delta_{film} \tag{25}$$

The newly exposed particle surface ($A_{cr} = l_{cr} w_{cr}$) will reform a new SEI film, of same thickness as film (δ_{film}), within a time frame of δt_{cr}. The current consumed to form new SEI layer is calculated in Eq. (26) using a similar formulation as Eq. (16) and (17).

$$i_{cr} = -\frac{A_{cr}\delta_{film}F\rho_{SEI}}{4\pi Rn^2 M_{SEI}\delta t_{cr}} \tag{26}$$

Here, the negative sign indicates lithium-ions being consumed to heal the cracked film. We assume that newly formed SEI layer would have the same thickness as the existing layer. This cracking current reduces the available exchange current for intercalation (Eq. 10). The electrical and mechanical properties for SEI and plated film are recorded in Table 2.

Table 2. Electrical and mechanical properties of film deposition on anode surface.

Properties	**SEI**	**Plated lithium**
Electrical conductivity, κ $(S\ m^{-1})$	5×10^{-6} [34]	1.1×10^{7} [47]
Elastic modulus, E (GPa)	0.43 [56]	7.82 [57]
Poisson's ratio, ν (1)	0.2 [22]	0.38 [57]
Ultimate tensile strength, σ_{1C} (MPa)	9.0 [56]	15.0 [58]
Critical film thickness, $\delta_{film,cr}$ (nm)	270 [59]	–
Surface energy, γ $(J\ m^{-2})$	13 [59]	–
Crack width, w_{cr} (nm)	10[ad]	–
SEI healing time, δt_{cr} (s)	1[ad]	–

[ad] Adjusted or assumed for the model

2.5 Capacity and efficiency model:

The reversible plating efficiency (Γ_{pl}) accounts for the irreversible lithium loss from the plated lithium film [25] during stripping process and is defined below in Eq. (27).

$$\Gamma_{pl} = \frac{\int_0^{t_r}(i_{st} + i_{cr} + i_{SEI})dt}{\int_0^{t_c} i_{pl}dt} \tag{27}$$

Consider that the SEI and cracking currents are of negative sign in the formulation and reduce the stripping current in Eq. (27). The relative capacity loss at the end of a charge cycle is formulated as follows in Eq. (28).

$$Q_{rel} = \frac{\int_0^{t_c+t_r} i_{el}dt}{\int_0^{t_c+t_r} i_{tot}dt} \tag{28}$$

3. Results and Discussion

The equations (1-18) underlying the single particle with electrolyte model are numerically solved using an Euler Implicit scheme in MATLAB 2019b for a NMC/C cell with an areal capacity of 0.6 mAh/cm^2. The model is simulated with the particle geometry and properties in Table 1, with a computational time step of 1 s. Unless otherwise mentioned, the initial SEI thickness is assumed to be 10 nm.

Experimental data from Ge et al. 2017 [36] is used to setup the initial conditions for the model. A constant current (CC) charging/discharging protocol is followed with 2000 sec of relaxation after each half cycle. The model predictions, based on the above-mentioned experimental parameters, are compared to reported measurements of voltage vs. time profile in Fig. 2 to demonstrate the validity of modeling assumptions and numerical implementation. The close agreement between the model predictions and experimental measurements indicate that the numerical implementation can approximate the battery'ss response.

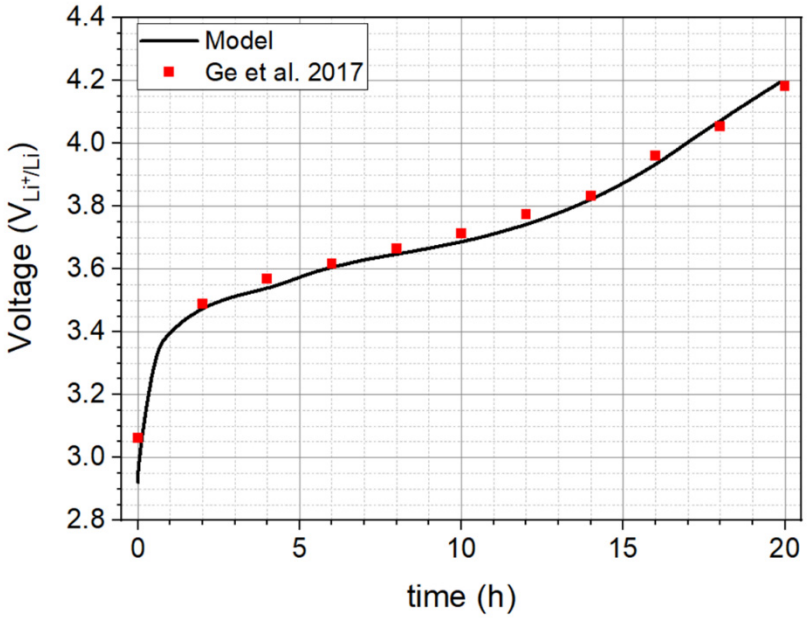

Figure 2. Validation of electrochemical model, Voltage vs. time predictions at C/20 and compared against Ge et al. 2017 [36].

The validated numerical code was utilized to predict the particle response during fast charging at the charging rate from 1 C to 6 C, and the computed anodic potential for all the charging rates are plotted in Fig. 3. As the charging rate is increased from 1 – 6 C, the anodic potential of the graphite particles starts to reduce (Fig. 3) and draws closer to 0 V. At 3 C rate of charging, the anodic potential becomes negative towards the end of the charging cycle. As the charging rate increases, the steeper concentration gradient in the anode forces the potential to become increasingly negative for a significantly longer fraction of the charging time period. Comparing 3 C to 6 C, the fraction of time for which plating occurs varies from 29% to 92%, respectively.

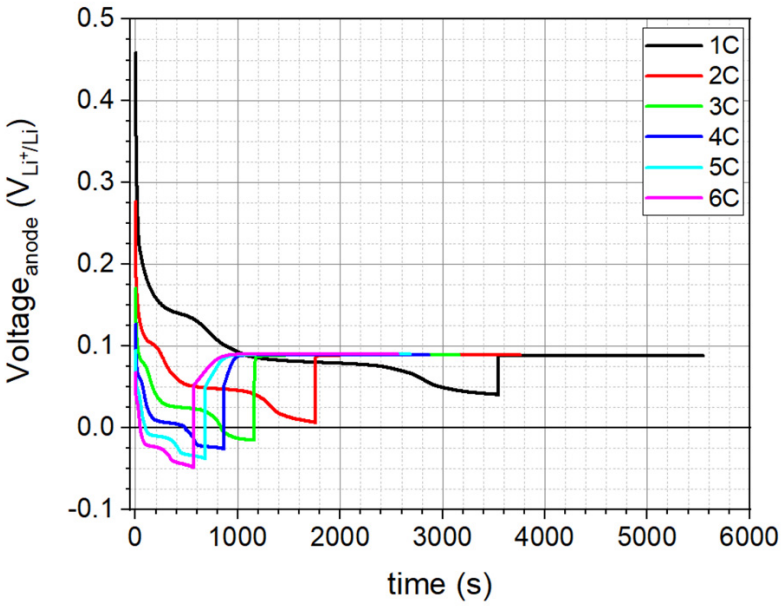

Figure 3. Anodic potential vs. time during charging half cycle for different charging rates.

During the relaxation period a voltage plateau is commonly observed in high charging rate experiments, which acts as an indicator for lithium plating/stripping phenomena. Fig. 4a shows the relaxation voltage vs. time (V-t) and Fig. 4b shows gradient of voltage vs. time curves for all six C-rates, and during the 600 s of relaxation period. From Fig. 3, it is found the plating mechanism would initiate from 3 C rate of charging and increase with charging rate. The V-t curves from 4 C to 6 C show a definite indication of voltage plateau and deviate from the 1 C and 2 C profile (Fig. 4a). The voltage plateaus occur because of re-intercallation of stripped lithium-ions into the anode

during the relaxation time-frame. The magnitude of the re-intercalating current, being very small compared to total input current during charging ($\sim 1/20$), is only able to create a small plateau in the voltage profile. For the 3 C charging rate, no significant deviation in the voltage profile is observed because the amount of lithium deposited is negligible.

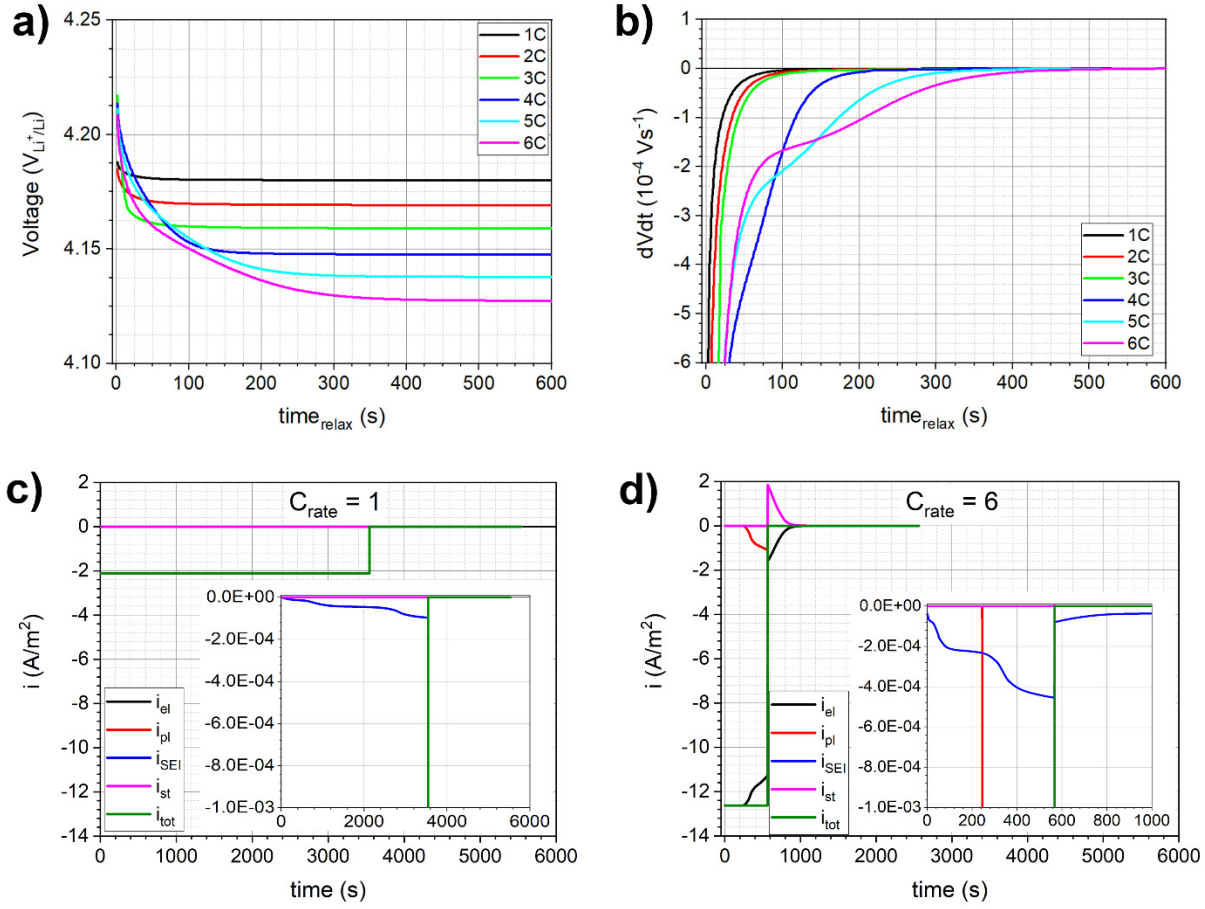

Figure 4. a) Voltage vs. time plot, and b) Voltage gradient vs. time plot for different charging rates during relaxation period, c) Current vs. time profile at 1 C charging condition during charging and relaxation period, and d) Current vs. time profile at 6 C charging condition during charging and relaxation period.

A more definitive representation of the voltage plateau and the effect of re-intercalating lithium-ion flux from stripped lithium are observed in the voltage gradient vs. time plots (dVdt-t) (Fig. 4b). The slope of the V-t plot changes direction when the plateau is initiated and smoothens over time as the lithium concentration in the particle relaxes. From 4C to 6 C the deflection in the dVdt-t plot shifts towards the right and increases in magnitude. The shifting of the deflection towards the right with broadening width indicates longer stripping duration which predicts plating

of more lithium. Furthermore, a steeper inflexion of the dVdt-t profile indicates more lithium-ions available for re-intercalation, again emphasizing increased lithium plating during charging process.

Computed components of the exchange current density (Eq. 10) – intercalation, SEI growth, plating, and stripping – are plotted for charging rates of 1C and 6C and relaxation after charging in Fig. 4c and 4d, respectively, to highlight the influence of negative anodic potential on anodic degradation process. At 1 C charging condition, the total exchange current density at the anode is split between the electrode intercalation current and SEI current densities. The lithium-ions available at the particle surface mostly contribute towards intercalation. Only a small fraction ($< 10^{-4}$) contributes to increasing the SEI overpotential leading to SEI growth (as observed from the zoomed inset plots in Fig. 4c and 4d). As there is no plated lithium on the anode surface, there is no stripping current during the relaxation period. The degradation mechanism at 1 C is found to be negligible with a steady but slow SEI growth.

The current vs. time variation for the 6 C case study (Fig. 4d) shows the total lithium-ion flux gets distributed between electrode, plating and SEI currents during the charging period ($t < 600\ s$). About 7.8% of the total exchange current is lost as plated lithium at the electrode surface, thus reducing the intercalation current considerably. During the relaxation period ($t > 600\ s$), the plated lithium gets stripped of providing a supply lithium-ion flux in the electrolyte. The stripped lithium either gets reversibly intercalated into the electrode or irreversibly reacts with the anode surface to form SEI. The irreversible component of the plated film is unavailable for further cycling of the battery and thus reduces the plating efficiency and cell capacity.

Predicted SEI and plating thickness during the different charging rates from 1 – 6 C and subsequent relaxation are plotted in Fig. 5a and 5b, respectively. With increasing of the plated current with C-rate, thicker plated lithium film deposits in the electrode/electrolyte interface (Fig. 5a). There is no lithium deposition for 1 C and 2 C because the anodic potential is positive (Fig.

3). The growth in the SEI film becomes interesting when coupled with plating/stripping mechanism (Fig. 5b). For 1 C and 2 C, we observe the conventional trend of SEI growth. The film grows during charging, when an external current is applied to charge the battery. The rate of SEI formation increases with C-rate during charging because more lithium-ions are available at the anode particle surface at higher C-rates. However, the total SEI thickness for 1 C charging was higher than 2 C because of constant current (CC) charging protocol. This is attributed to the smaller charging time in 2 C compared to 1 C under the CC protocol. During relaxation (when the applied current is made zero) for the charging rates of 1C and 2C, the SEI growth stops and the film thickness becomes stagnant. However, during relaxation for charging at rates of 4 C – 6 C, the SEI growth profile changes because of coupling between lithium plating/stripping currents and SEI deposition. During the relaxation period, the stripping current contributes to the SEI growth (refer Fig. 4d). Therefore at faster charging rates, the SEI keeps growing in the relaxation period adding to irreversible lithium loss.

The evolution of the electrical resistance of SEI film is modeled using micromechanical models in Eq. 19 and plotted in Fig. 5c during the charging at rates of 1 C – 6 C and subsequent relaxation. At charging rates of 1C and 2C, there is no lithium plating and thus the resistance of SEI film monotonically increases with an increase in thickness. As lithium plates during faster charging rates, it creates conductive pathways through the film, thereby reducing the film resistance. As the volume fraction of plated lithium deposited during charging increases with C-rate, the film resistance decreases (Fig. 5c). During relaxation, the resistance is recovered as the deposited lithium strips off the film. For 3 C, the film resistance after relaxation is slightly greater than after end of charging because new SEI is formed during the stripping process. For 4 C – 6 C, the film resistance is not completely recovered as some dead lithium gets trapped between SEI layers during deposition, which does not get stripped (Fig. 5d). The areal dead lithium mass can be converted to areal capacity loss from dead lithium using formulation ($Q_{dead} =$

$m_{pl,dead}/0.3\ \left[gm/(\frac{gm}{1000mAh})\right]$). The dead lithium deposition increases with C-rate, which contributes to irreversible loss and reduction in the Γ_{pl}.

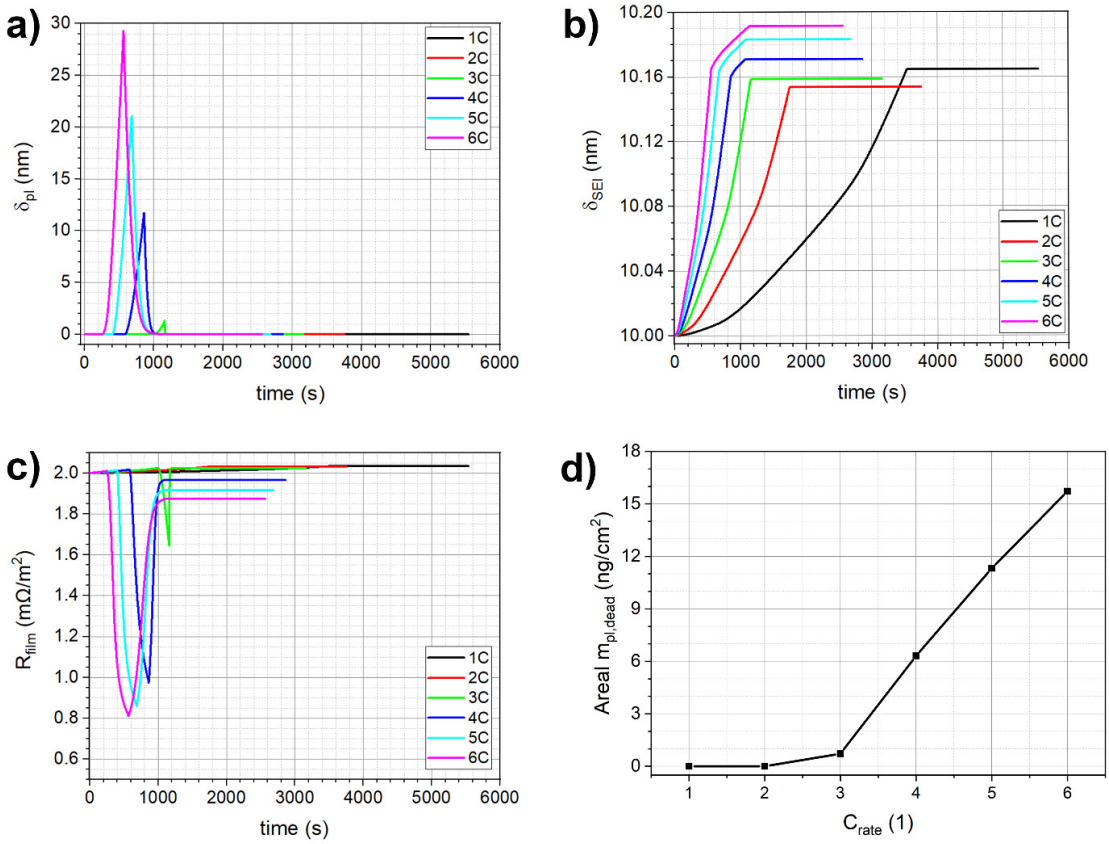

Figure 5. Film growth predicitions for different charging conditions, a) Plated lithium film thickness vs. time, b) SEI film thickness vs. time, c) Film resistance vs. time, and d) Areal mass of dead lithium stored in film vs. C-rate.

The plating volume fraction increases with the increment in lithium deposition at higher C-rates (Fig. 6a). The change in plating volume fraction in the SEI film (matrix) during charging and relaxation determines the mechanical response of the film (Fig. 1c) and Equations 19 – 21. The presence of lithium metal reduces the ultimate strength and increases the stiffness of the film. The film stress in the SEI film increases during charging as the anode particle expands (Fig. 6b). The expanding particle induces a tensile (positive) hoop stress on to the film. Increasing the charging rate creates a larger concentration gradient in the particle, thus increasing the surface hoop strain and stress in the film. Below 3 C, the film stress increases to maximum during charging and then stabilizes during relaxation period. For 3 C and beyond, a spike in the stress profile is

observed during the plating and stripping period. During the plating process, the stiffness of the SEI film increases (Fig. 1c), causing a faster rise in the film stress during particle expansion. During relaxation, the particle expands marginally due to re-intercalating lithium-ions from the stripped lithium adding to the hoop stress. As the plated lithium strips from the anode film, the film stiffness, and consequently the film stress, reduces.

When the strain energy in the strained film exceeds the critical strain energy, the film cracks. Fig. 6c shows the film strain energy ($G_{1,film}$) vs. time at different C-rates. The spike in the stress profile observed in Fig. 6b during periods of charging and stripping causes a significant increase in the stress intensity of the composite film. Comparing the ratio of film strain to critical strain energy vs. time at different charging rates (Fig. 6d), we can predict the condition of film fracture and crack propoagation. For C-rate < 3 C, the strain energy of the film does not exceed critical value and hence no film cracking is observed. Plated lithium in the film decreases the critical energy in the film, thus making it prone to fracture. Beyond 3 C loading, the strain energy in the film during the plating domain exceeds the critical energy indicating fracture in the film. The opening of the fracture releases the strain energy and relieves the film stress. The film cracks through the SEI (matrix phase) and opens up new electrode surface for reaction with electrolyte. In order to model the consumption of active lithium due to passive SEI film reformation on the exposed surface, an additional irreversible parasitic term is added to the exchange current density in Eq. 20. The cracking current would absorb lithium stripped of the plated film as observed in Fig. 6e. This would result in a reduction in the efficiency and capacity of the battery as will be discussed in a later section. Computed components for the current vs. time in Eq. 10, incorporating the influence of film cracking, are plotted in Fig. 6f (zoomed inset to show the SEI current during charging and relaxation) for charging rate of 6 C. The comparison of the current profiles in presence of cracking (Fig. 6f) and no-cracking (Fig. 4d) shows that as soon as new film forms, the SEI regains its stressed state and becomes prone to cracking. The film cracking would continue

even during the relaxation period till the strain energy in the film becomes lower than the critical energy.

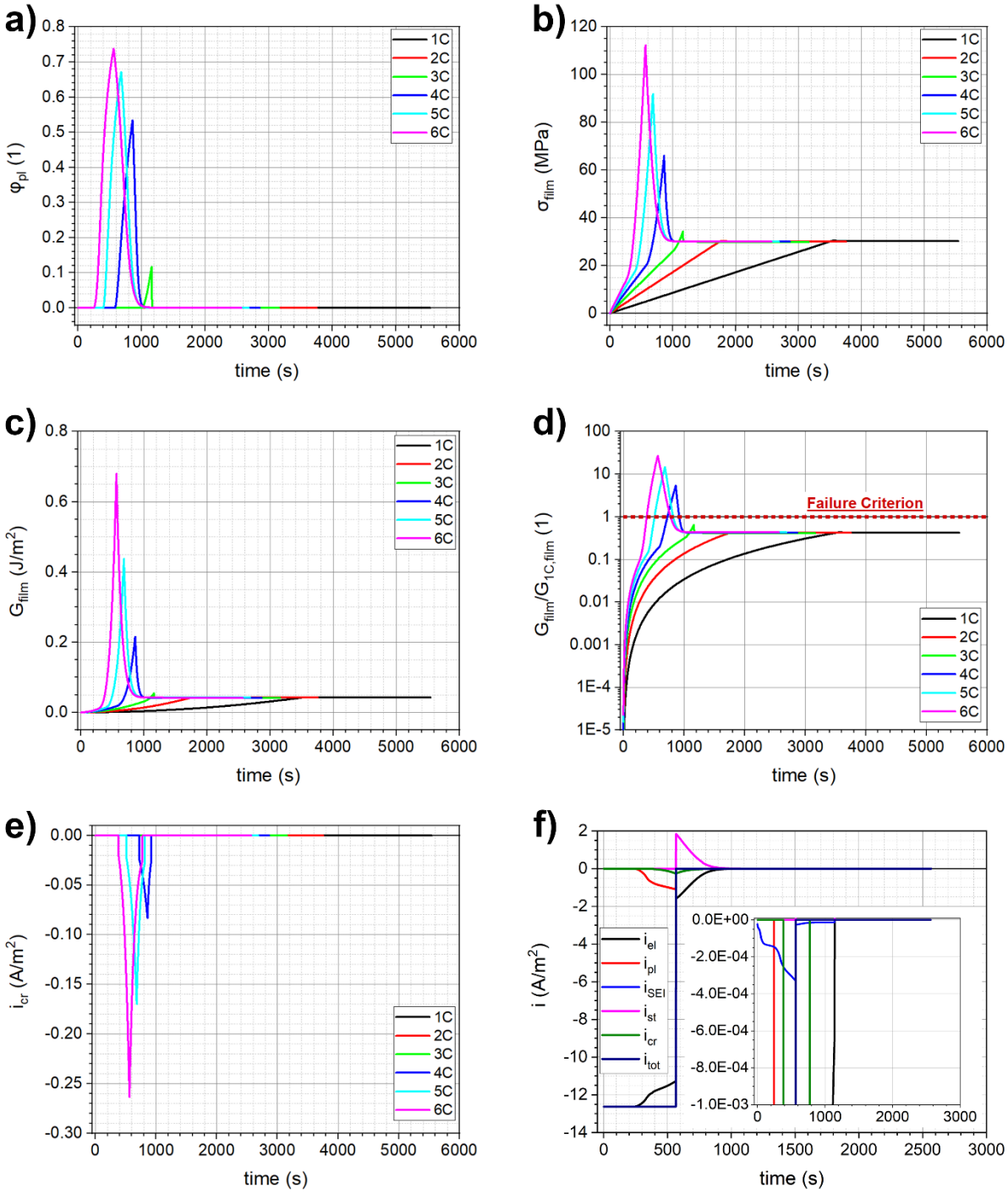

Figure 6. a) Lithium plating phase volume vs. time, b) Film hoop stress vs. time, c) Strain energy for the SEI + plated film vs. time at different C-rates, d) Normalized film strain energy vs. time at different C-rates, e) Cracking current vs. time at different charging conditions, f) Current components vs. time at 6 C.

As the hoop stress in the film increases with the C-rate, the crack length (l_{cr}) increases, thus exposing more electrode surface and extracting a larger cracking current. The crack length acts as a measure of the propensity of degradation and loss in the battery. A contour map is presented in Fig. 7 providing a trend for the cracking propensity with C-rate and SEI thickness. The SEI film thickness indicates the stage of battery operation, i.e. number of charge/discharge cycles. The map is divided in four broad sections. First, for low C-rate ($\leq$ 3 C) and thin SEI film ($<$ 20 nm), the cracking tendency is small (almost negligible) because the strain energy in the film is negligible. The cracking tendency increases towards a maximum at critical strain energy. Furthermore, no plating at low C-rates results in no degradation of the mechanical integrity of the film. Second, for high C-rates ($>$ 3 C) and thin SEI film ($<$ 20 nm), the cracking tendency is very high because excessive plating at larger C-rate would induce a high-volume fraction of plated lithium in the SEI film. This severely compromises the mechanical integrity of the film and causes an increased fracture propensity. Third, for high C-rates ($>$ 3 C) and thicker SEI films ($>$ 20 nm), the propensity of fracture reduces because the volume fraction of plated material reduces, thus making it mechanically stronger. Finally at low C-rates, once the strain energy release rates exceed a critical value corresponding to thickness (> 20 nm), the cracking propensity gradually decreases with increasing film thickness because thicker SEI film provides a stronger resistance to fracture. The simulation predicts a decrease in cracking tendency, hence decrease in crack length (l_{cr}) by 5% with the SEI thickness increasing from 20 nm to 100 nm. Therefore, ageing of the lithium battery or pre-deposition of a thicker SEI layer may improve the mechanical integrity of the battery and reduce losses due to SEI cracking.

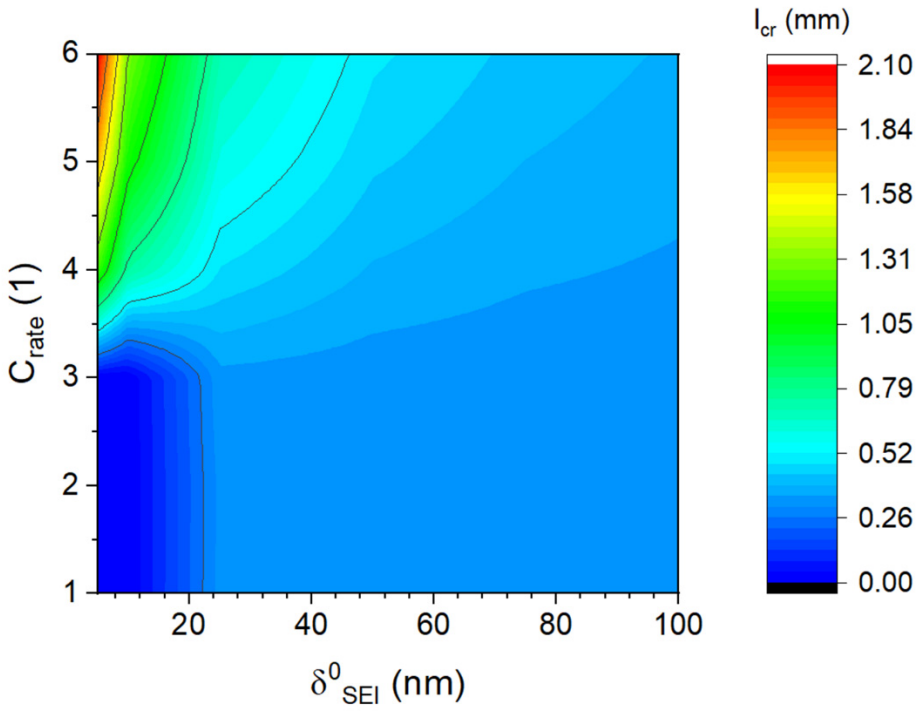

Figure 7. Crack length contour map over different C-rate and initial SEI thickness.

The plating efficiency for plating mechanism accounts for the irreversible loss of plated lithium during stripping process. Fig. 8a compares Γ_{pl} of the battery simulated at 6 C at different stages of battery life (or SEI thickness) considering losses with/without SEI cracking. Dead lithium storage, SEI growth and crack healing with new SEI are the primary forms of irreversible processes contributing to anodic degradation and loss of Γ_{pl}. Without considering film cracking and for the same dead lithium storage, the change in SEI thickness does not incur any significant change in the efficiency with which the plating film strips. The SEI current contribution is negligible and does not change considerably with cycling or SEI growth.

If SEI cracking is considered, low Γ_{pl} is observed at low SEI thickness because thin films would propagate significant cracking (Fig. 6f), which would absorb considerable lithium-ion flux to reform new SEI film on cracked surfaces. The cracking stabilizes as the SEI thickness increases, and around 20 nm, a maximum in Γ_{pl} (or minimum loss) is observed. For thicker SEI films, the overall cracking length (l_{cr}) reduces (Fig. 6f). However, the net volume of new SEI film increases

($V_{cr} = l_{cr} w_{cr} \delta_{film}$), therefore drawing more current from electrolyte to heal the film. This causes a slight reduction in the Γ_{pl} at later stages of battery life cycle.

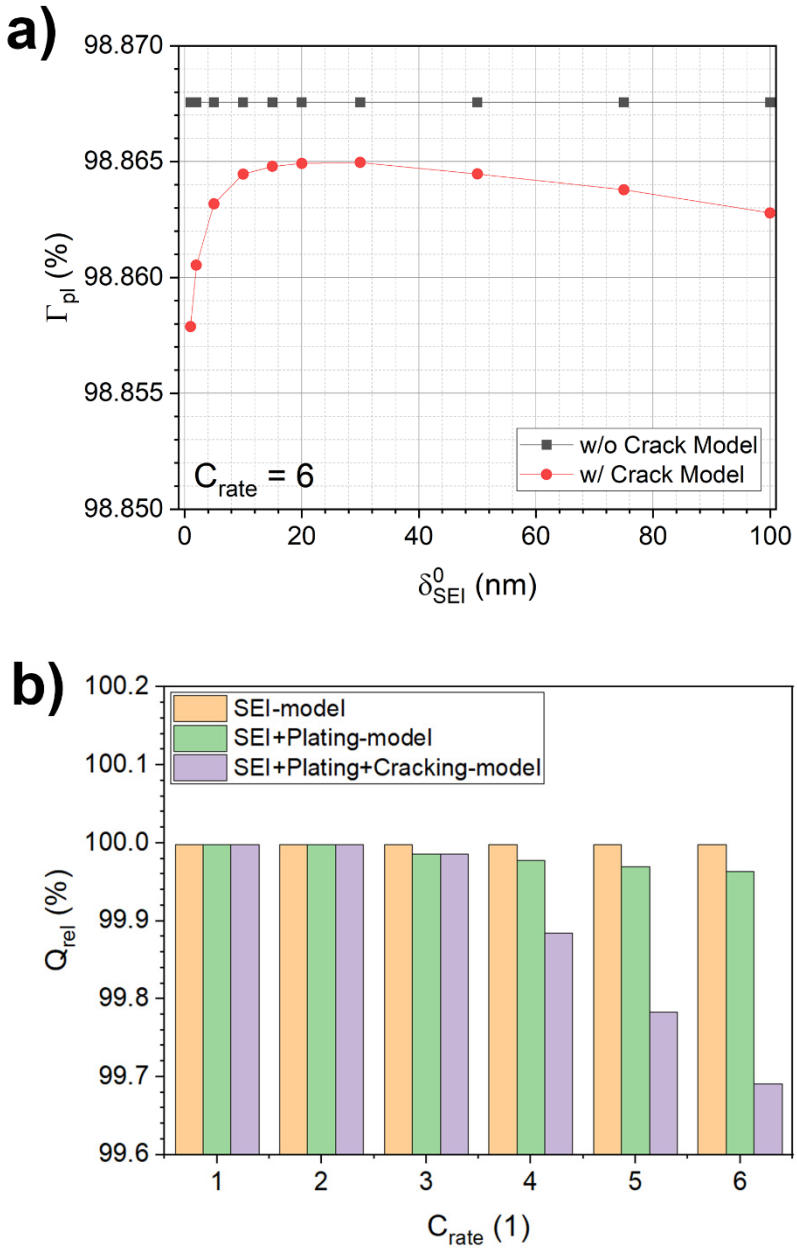

Figure 8. a) plating efficiency vs. initial SEI thickness with/without cracking considered, and b) Relative capacity vs. C-rate considering SEI-only, SEI + Plating and SEI + Plating + Film cracking models.

The relative capacity at the end of one cycle is compared at different C-rates assuming only SEI, SEI+plating and SEI+plating+cracking models in Fig. 8b. For 1 C and 2 C, there is no lithium

plating or film cracking. So, the SEI based degradation model predicts the relative capacity of 99.998% with or without plating and cracking. At 3 C condition, lithium plating initiates (Fig. 3), so the SEI-only model overpredicts the relative capacity. SEI with plating model considers the losses due to dead-lithium and SEI growth during stripping period and predicts a more realistic capacity (~99.986%). Since the SEI film ($\delta_{SEI}^{0} = 10\,nm$) does not crack under such loading conditions, the cracking model can be ignored. For C-rates higher than 3 C, all three failure mechanisms are present and contribute towards battery degradation. For 6 C, by considering all mechanisms Q_{rel} is found 99.691% compared to 99.964% and 99.994% with SEI+plating and SEI-only models, respectively. Therefore, depending on the charging conditions and stage of cycle life, an accurate relative capacity prediction requires the consideration of the possibility of plating and cracking within SEI layers. Electrode geometry and particle morphology are also important parameters.

4. Conclusion

We have reported an anodic degradation model that couples SEI growth with lithium plating/stripping, dead-lithium storage, and SEI film cracking for prediction of the battery capacity. Model accounts for the synergistic coupling of different degradation mechanisms at high C-rates and their influence on battery capacity. Results show that negative anodic potential results in lithium plating during charging. During relaxation after charging, plated lithium may be stripped either through reversible or irreversible reactions. Modes for irreversible loss due to dead-lithium storage and SEI formation was formulated. Fracture mechanics analysis of the SEI film was used to predict the condition of SEI fracture. Thicker SEI film and lower C-rates were found to reduce the tendency of film cracking while thinner SEI films and high C-rates were found to increase the possibility of fracture. Plating coloumbic efficiency was computed to quantify the irreversible loss from the plating and stripping processes. For low charging conditions, only SEI growth-based degradation model was sufficient to predict battery capacity decay. However, at higher charging rates, SEI growth along with plating and SEI cracking mechanisms needs to be incorporated into

the degradation models for accurate prediction of relative capacity. The coupled mechano-chemical model developed in this study may help in identifying the parameters and mitigating the conditions that lead to anodic degradation during fast-charging of lithium-ion batteries.

5. Nomenclature

Ω_n	Anode partial molar volume	α	Butler Volmer parameter
G_1	Strain energy	γ	Surface energy
G_{1C}	Critical strain energy	δ	Film thickness
Q_{rel}	Relative capacity	δt_{cr}	Crack healing time
$\mathbb{R}_{film}$	Film resistance	η	Electrode potential
l_{cr}	Crack length	κ	Electrical conductivity
w_{cr}	Crack width	$\bar{\nu}$	Plane strain Poisson's ratio
σ_c	Ultimate tensile strength	ξ	Dead-lithium mass fraction
$\mathcal{R}$	Gas Constant	ρ	Density
Φ	Solid/Electrolyte potential	σ	Film stress
Γ	Plating efficiency	ϕ	Volume fraction
D	Diffusion coefficient	Subscripts	
$\bar{E}$	Plane strain elastic modulus		
F	Faraday's constant	EC	Ethylene carbonate
I	Current density	SEI	Solid electrolyte interface
M	Molar mass	c	Charging period
R	Particle radius	e	Liquid (electrolyte) phase
T	Cell temperature	el	Electrode
U	Open circuit potential	$film$	Film
a	Gradient parameter	max	Maximum
c	Lithium-ion concentration	n	Negative electrode
i	Exchange current density	p	Positive electrode
k	Reaction rate constant	pl	Plated film
m	Film mass	r	Relaxation period

Acknowledgement:

This work was supported by the Critical Materials Institute, an Energy Innovation Hub funded by the U.S. Department of Energy, Office of Energy Efficiency and Renewable Energy, Advanced Manufacturing Office. This work was also supported by the Department of Energy, Laboratory Directed Research and Development program at Ames Laboratory. Ames Laboratory is operated for the U.S. Department of Energy by Iowa State University of Science and Technology under Contract No. DE-AC02-07CH11358.

References:

[1] J.B. Goodenough, K.-S. Park, The Li-Ion Rechargeable Battery: A Perspective, J. Am. Chem. Soc. 135 (2013) 1167–1176. https://doi.org/10.1021/ja3091438.

[2] C.-X. Zu, H. Li, Thermodynamic analysis on energy densities of batteries, Energy Environ. Sci. 4 (2011) 2614. https://doi.org/10.1039/c0ee00777c.

[3] V. Etacheri, R. Marom, R. Elazari, G. Salitra, D. Aurbach, Challenges in the development of advanced Li-ion batteries: a review, Energy Environ. Sci. 4 (2011) 3243. https://doi.org/10.1039/c1ee01598b.

[4] M.M. Thackeray, C. Wolverton, E.D. Isaacs, Electrical energy storage for transportation—approaching the limits of, and going beyond, lithium-ion batteries, Energy Environ. Sci. 5 (2012) 7854. https://doi.org/10.1039/c2ee21892e.

[5] J.M. Tarascon, M. Armand, Issues and challenges facing rechargeable lithium batteries, Nature. 414 (2001) 359–367. https://doi.org/10.1038/35104644.

[6] M. Armand, J.-M. Tarascon, Building better batteries, Nature. 451 (2008) 652.

[7] J. Vetter, P. Novák, M.R. Wagner, C. Veit, K.-C. Möller, J.O. Besenhard, M. Winter, M. Wohlfahrt-Mehrens, C. Vogler, A. Hammouche, Ageing mechanisms in lithium-ion batteries, J. Power Sources. 147 (2005) 269–281. https://doi.org/10.1016/j.jpowsour.2005.01.006.

[8] A. Barré, B. Deguilhem, S. Grolleau, M. Gérard, F. Suard, D. Riu, A review on lithium-ion battery ageing mechanisms and estimations for automotive applications, J. Power Sources. 241 (2013) 680–689. https://doi.org/10.1016/j.jpowsour.2013.05.040.

[9] L. Ma, M. Nie, J. Xia, J.R. Dahn, A systematic study on the reactivity of different grades of charged Li[NixMnyCoz]O2 with electrolyte at elevated temperatures using accelerating rate calorimetry, J. Power Sources. 327 (2016) 145–150. https://doi.org/10.1016/j.jpowsour.2016.07.039.

[10] Q. Liu, C. Du, B. Shen, P. Zuo, X. Cheng, Y. Ma, G. Yin, Y. Gao, Understanding undesirable anode lithium plating issues in lithium-ion batteries, RSC Adv. 6 (2016) 88683–88700. https://doi.org/10.1039/C6RA19482F.

[11] N. Kim, S. Chae, J. Ma, M. Ko, J. Cho, Fast-charging high-energy lithium-ion batteries via implantation of amorphous silicon nanolayer in edge-plane activated graphite anodes, Nat. Commun. 8 (2017). https://doi.org/10.1038/s41467-017-00973-y.

[12] A.N. Dey, B.P. Sullivan, The Electrochemical Decomposition of Propylene Carbonate on Graphite, J. Electrochem. Soc. 117 (1970) 222. https://doi.org/10.1149/1.2407470.

[13] E. Peled, The Electrochemical Behavior of Alkali and Alkaline Earth Metals in Nonaqueous Battery Systems—The Solid Electrolyte Interphase Model, J. Electrochem. Soc. 126 (1979) 2047. https://doi.org/10.1149/1.2128859.

[14] E. Peled, D. Golodnitsky, G. Ardel, Advanced Model for Solid Electrolyte Interphase Electrodes in Liquid and Polymer Electrolytes, J. Electrochem. Soc. 144 (1997) L208–L210. https://doi.org/10.1149/1.1837858.

[15] D. Aurbach, B. Markovsky, M.. Levi, E. Levi, A. Schechter, M. Moshkovich, Y. Cohen,

New insights into the interactions between electrode materials and electrolyte solutions for advanced nonaqueous batteries, J. Power Sources. 81–82 (1999) 95–111. https://doi.org/10.1016/S0378-7753(99)00187-1.

[16] M. Winter, The Solid Electrolyte Interphase – The Most Important and the Least Understood Solid Electrolyte in Rechargeable Li Batteries, Zeitschrift Für Phys. Chemie. 223 (2009) 1395–1406. https://doi.org/10.1524/zpch.2009.6086.

[17] P. Verma, P. Maire, P. Novák, A review of the features and analyses of the solid electrolyte interphase in Li-ion batteries, Electrochim. Acta. 55 (2010) 6332–6341. https://doi.org/10.1016/j.electacta.2010.05.072.

[18] S.J. An, J. Li, C. Daniel, D. Mohanty, S. Nagpure, D.L. Wood, The state of understanding of the lithium-ion-battery graphite solid electrolyte interphase (SEI) and its relationship to formation cycling, Carbon N. Y. 105 (2016) 52–76. https://doi.org/10.1016/j.carbon.2016.04.008.

[19] D. Zhao, J. Wang, H. Lu, P. Wang, H. Liu, S. Li, Tailoring interfacial architecture of high-voltage cathode with lithium difluoro(bisoxalato) phosphate for high energy density battery, J. Power Sources. 456 (2020) 228006. https://doi.org/10.1016/j.jpowsour.2020.228006.

[20] D. Zhao, J. Wang, P. Wang, H. Liu, S. Li, Regulating the composition distribution of layered SEI film on Li-ion battery anode by LiDFBOP, Electrochim. Acta. 337 (2020) 135745. https://doi.org/10.1016/j.electacta.2020.135745.

[21] X. Zhang, A.M. Sastry, W. Shyy, Intercalation-induced stress and heat generation within single lithium-ion battery cathode particles, J. Electrochem. Soc. 155 (2008) A542--A552.

[22] I. Laresgoiti, S. Käbitz, M. Ecker, D.U. Sauer, Modeling mechanical degradation in lithium ion batteries during cycling: Solid electrolyte interphase fracture, J. Power Sources. 300 (2015) 112–122. https://doi.org/10.1016/j.jpowsour.2015.09.033.

[23] R.D. Deshpande, D.M. Bernardi, Modeling Solid-Electrolyte Interphase (SEI) Fracture: Coupled Mechanical/Chemical Degradation of the Lithium Ion Battery, J. Electrochem. Soc. 164 (2017) A461–A474. https://doi.org/10.1149/2.0841702jes.

[24] A.J. Smith, J.C. Burns, J.R. Dahn, A High Precision Study of the Coulombic Efficiency of Li-Ion Batteries, Electrochem. Solid-State Lett. 13 (2010) A177. https://doi.org/10.1149/1.3487637.

[25] L.E. Downie, L.J. Krause, J.C. Burns, L.D. Jensen, V.L. Chevrier, J.R. Dahn, In Situ Detection of Lithium Plating on Graphite Electrodes by Electrochemical Calorimetry, J. Electrochem. Soc. 160 (2013) A588–A594. https://doi.org/10.1149/2.049304jes.

[26] J.C. Burns, D.A. Stevens, J.R. Dahn, In-Situ Detection of Lithium Plating Using High Precision Coulometry, J. Electrochem. Soc. 162 (2015) A959–A964. https://doi.org/10.1149/2.0621506jes.

[27] S. Solchenbach, D. Pritzl, E.J.Y. Kong, J. Landesfeind, H.A. Gasteiger, A Gold Micro-Reference Electrode for Impedance and Potential Measurements in Lithium Ion Batteries, J. Electrochem. Soc. 163 (2016) A2265–A2272. https://doi.org/10.1149/2.0581610jes.

[28] S.J. An, J. Li, C. Daniel, S. Kalnaus, D.L. Wood, Design and Demonstration of Three-Electrode Pouch Cells for Lithium-Ion Batteries, J. Electrochem. Soc. 164 (2017) A1755–

A1764. https://doi.org/10.1149/2.0031709jes.

[29] R. V. Bugga, M.C. Smart, Lithium Plating Behavior in Lithium-Ion Cells, ECS Trans. 25 (2019) 241–252. https://doi.org/10.1149/1.3393860.

[30] M.C. Smart, B. V. Ratnakumar, Effects of Electrolyte Composition on Lithium Plating in Lithium-Ion Cells, J. Electrochem. Soc. 158 (2011) A379. https://doi.org/10.1149/1.3544439.

[31] V. Agubra, J. Fergus, Lithium Ion Battery Anode Aging Mechanisms, Materials (Basel). 6 (2013) 1310–1325. https://doi.org/10.3390/ma6041310.

[32] M. Petzl, M.A. Danzer, Nondestructive detection, characterization, and quantification of lithium plating in commercial lithium-ion batteries, J. Power Sources. 254 (2014) 80–87. https://doi.org/10.1016/j.jpowsour.2013.12.060.

[33] M. Petzl, M. Kasper, M.A. Danzer, Lithium plating in a commercial lithium-ion battery – A low-temperature aging study, J. Power Sources. 275 (2015) 799–807. https://doi.org/10.1016/j.jpowsour.2014.11.065.

[34] X.G. Yang, Y. Leng, G. Zhang, S. Ge, C.Y. Wang, Modeling of lithium plating induced aging of lithium-ion batteries: Transition from linear to nonlinear aging, J. Power Sources. (2017). https://doi.org/10.1016/j.jpowsour.2017.05.110.

[35] X.-G. Yang, S. Ge, T. Liu, Y. Leng, C.-Y. Wang, A look into the voltage plateau signal for detection and quantification of lithium plating in lithium-ion cells, J. Power Sources. 395 (2018) 251–261. https://doi.org/10.1016/j.jpowsour.2018.05.073.

[36] H. Ge, T. Aoki, N. Ikeda, S. Suga, T. Isobe, Z. Li, Y. Tabuchi, J. Zhang, Investigating Lithium Plating in Lithium-Ion Batteries at Low Temperatures Using Electrochemical Model with NMR Assisted Parameterization, J. Electrochem. Soc. 164 (2017) A1050–A1060. https://doi.org/10.1149/2.0461706jes.

[37] D. Ren, K. Smith, D. Guo, X. Han, X. Feng, L. Lu, M. Ouyang, J. Li, Investigation of Lithium Plating-Stripping Process in Li-Ion Batteries at Low Temperature Using an Electrochemical Model, J. Electrochem. Soc. 165 (2018) A2167–A2178. https://doi.org/10.1149/2.0661810jes.

[38] X. Zhao, Y. Yin, Y. Hu, S.-Y. Choe, Electrochemical-thermal modeling of lithium plating/stripping of Li(Ni0.6Mn0.2Co0.2)O2/Carbon lithium-ion batteries at subzero ambient temperatures, J. Power Sources. 418 (2019) 61–73. https://doi.org/10.1016/j.jpowsour.2019.02.001.

[39] D. Müller, T. Dufaux, K.P. Birke, Model-Based Investigation of Porosity Profiles in Graphite Anodes Regarding Sudden-Death and Second-Life of Lithium Ion Cells, Batteries. 5 (2019) 49. https://doi.org/10.3390/batteries5020049.

[40] X. Hu, L. Xu, X. Lin, M. Pecht, Battery Lifetime Prognostics, Joule. 4 (2020) 310–346. https://doi.org/10.1016/j.joule.2019.11.018.

[41] S.J. Moura, F.B. Argomedo, R. Klein, A. Mirtabatabaei, M. Krstic, Battery State Estimation for a Single Particle Model With Electrolyte Dynamics, IEEE Trans. Control Syst. Technol. 25 (2017) 453–468. https://doi.org/10.1109/TCST.2016.2571663.

[42] A.J. Bard, L.R. Faulkner, Electrochemical Methods Fundamentals of Electrochemistry, 2001. https://doi.org/10.1016/B978-0-08-098353-0.00003-8.

[43] M. Safari, M. Morcrette, A. Teyssot, C. Delacourt, Multimodal Physics-Based Aging Model for Life Prediction of Li-Ion Batteries, J. Electrochem. Soc. 156 (2009) A145. https://doi.org/10.1149/1.3043429.

[44] C. von Lüders, J. Keil, M. Webersberger, A. Jossen, Modeling of lithium plating and lithium stripping in lithium-ion batteries, J. Power Sources. 414 (2019) 41–47. https://doi.org/10.1016/j.jpowsour.2018.12.084.

[45] R. Deshpande, M. Verbrugge, Y.-T. Cheng, J. Wang, P. Liu, Battery Cycle Life Prediction with Coupled Chemical Degradation and Fatigue Mechanics, J. Electrochem. Soc. 159 (2012) A1730–A1738. https://doi.org/10.1149/2.049210jes.

[46] L. Benitez, J.M. Seminario, Ion Diffusivity through the Solid Electrolyte Interphase in Lithium-Ion Batteries, J. Electrochem. Soc. 164 (2017) E3159–E3170. https://doi.org/10.1149/2.0181711jes.

[47] T. Gray, M. Whitby, N. Mann, Technical data for Lithium, (n.d.).

[48] G. Bieker, M. Winter, P. Bieker, Electrochemical in situ investigations of SEI and dendrite formation on the lithium metal anode, Phys. Chem. Chem. Phys. 17 (2015) 8670–8679. https://doi.org/10.1039/C4CP05865H.

[49] S.P. Rangarajan, Y. Barsukov, P.P. Mukherjee, In operando signature and quantification of lithium plating, J. Mater. Chem. A. 7 (2019) 20683–20695. https://doi.org/10.1039/C9TA07314K.

[50] W. Callister, D. Rethwisch, Materials Science & Engineering. Chapter 16: Composite Materials, 2014. https://doi.org/10.1109/MCISE.2001.963423.

[51] M. Taya, Electronic Composites, Cambridge University Press, 2005. https://doi.org/10.1017/CBO9780511550508.

[52] Z. Hashin, S. Shtrikman, A variational approach to the theory of the elastic behaviour of polycrystals, J. Mech. Phys. Solids. 10 (1962) 343–352. https://doi.org/10.1016/0022-5096(62)90005-4.

[53] J. Cai, W. Wei, X. Hu, D.A. Wood, Electrical conductivity models in saturated porous media: A review, Earth-Science Rev. 171 (2017) 419–433. https://doi.org/10.1016/j.earscirev.2017.06.013.

[54] G. Eckold, Design and Manufacture of Composite Structures, Woodhead Publishing Limited, Cambridge, England, 1994. https://doi.org/10.1533/9781845698560.

[55] L.B. Freund, S. Suresh, Thin Film Materials, Cambridge University Press, New York, 2004. https://doi.org/10.1017/CBO9780511754715.

[56] I. Yoon, S. Jurng, D.P. Abraham, B.L. Lucht, P.R. Guduru, Measurement of mechanical and fracture properties of solid electrolyte interphase on lithium metal anodes in lithium ion batteries, Energy Storage Mater. 25 (2020) 296–304. https://doi.org/10.1016/j.ensm.2019.10.009.

[57] A. Masias, N. Felten, R. Garcia-Mendez, J. Wolfenstine, J. Sakamoto, Elastic, plastic, and

creep mechanical properties of lithium metal, J. Mater. Sci. 54 (2019) 2585–2600. https://doi.org/10.1007/s10853-018-2971-3.

[58] Ryan P Schultz, Lithium: Measurement of Young's Modulus and Yield Strength, Batavia, IL, IL, 2002. https://doi.org/10.2172/804180.

[59] R. Kumar, A. Tokranov, B.W. Sheldon, X. Xiao, Z. Huang, C. Li, T. Mueller, In Situ and Operando Investigations of Failure Mechanisms of the Solid Electrolyte Interphase on Silicon Electrodes, ACS Energy Lett. 1 (2016) 689–697. https://doi.org/10.1021/acsenergylett.6b00284.